Study on vertical vibration and transmission characteristics of railway ballast using impact hammer test

Liu, Ganzhong; Cong, Jianli ; Wang, Ping; Du, Shuai ; Wang, Li; Chen, Rong

DOI
10.1016/j.conbuildmat.2021.125898

Publication date
2022

Document Version
Final published version

Published in
Construction and Building Materials

Construction and Building Materials 316 (2022) 125898

Contents lists available at ScienceDirect

Construction and Building Materials

journal homepage: www.elsevier.com/locate/conbuildmat

Study on vertical vibration and transmission characteristics of railway ballast using impact hammer test

Ganzhong Liu [a,b], Jianli Cong [a,b], Ping Wang [a,b], Shuai Du [a,b], Li Wang [a,c], Rong Chen [a,b,*]

[a] MOE Key Laboratory of High-speed Railway Engineering, Southwest Jiaotong University, Chengdu, China
[b] School of Civil Engineering, Southwest Jiaotong University, Chengdu, China
[c] Section of Railway Engineering, Department of Engineering Structures, Faculty of Civil Engineering and Geosciences, Delft University of Technology, Delft, the Netherlands

ARTICLE INFO

Keywords:
Ballast
Vibration
Discrete element
Transmission
Natural frequency
Damping

ABSTRACT

The vertical vibration and transmission characteristics of ballast are key factors that affect the dynamic stability of railway track structures and control the settlement of ballasted beds. Therefore, the following study was conducted to explore this topic. Firstly, through an impact hammer test on a ballast sensor with embedding chip, the vertical vibration data of the ballast was accurately measured. Therefore, the vertical vibration characteristics of a single ballast can be studied. Then, the vertical vibration characteristics at different positions in the stack were obtained by embedding ballast sensors into a ballasted stack. Finally, combined with field tests, a discrete element numerical model was established, then the vibration transmission speed and diffusion angle in a ballasted stack were calculated. The results of this study show that the damping ratio of ballast particles is less than 0.1, and the natural frequency is above 1000 Hz. The damping ratio and natural frequency of ballasts are greatly affected by their shape. The damping ratio of a ballasted stack is greater than that of ballast particles, and its natural frequency is lower. This indicates that the ballasted stack has the attributes of a soft material. The vertical acceleration transmission rate of ballasts is lower at frequencies below 257.94 Hz. This shows that the vibration suppression ability of the ballasted bed is better in the lower frequency range. As the depth increases, the vertical vibration transmission speed of the ballast gradually decreases, as does the accumulated external force. In the impact hammer test of a ballasted box, the average vertical vibration transmission speed was calculated to be 0.88 mm/μs, and the ballast vibration was transmitted downward at a diffusion angle of 35.32°–54.51° from the direction of gravity.

1. Introduction

Due to their short construction period, ease of maintenance, good damping performance, easy drainage, and superior cost effectiveness, ballasted railway tracks are widely used in high-speed railways [1]. However, the ballasted track structure consists of a large stack of gravel particles, and it exhibits pronounced combinational and discrete characteristics. The passage of a high-speed train causes vigorous wheel-rail interaction and generates violent vibration of the ballasted bed. The stimulation of the vibration causes significant changes in the material properties, topological structure, and nesting of the ballast particles, which can profoundly affect the macroscopic vibration transfer behavior and microscopic mechanical mechanism of a ballasted bed over extended periods of service [2]. Therefore, the study of the vertical vibration and transmission characteristics of railway ballast is important to the design, operation, and maintenance of ballasted track.

There have been extensive studies on the vibration characteristics of ballasted stacks. Shahin et al. [3] and Li et al. [4] analyzed the vibration characteristics of the ballast layer of railway tracks by viewing them as an elastic continuum based on the theory of continuum mechanics, and proposed important concepts for ballast layers, such as Rayleigh waves and key velocity ranges. Zhai et al. [5] advanced the theory and method of vehicle-track coupling dynamics using differential equations and modal decomposition methods, and regarded a ballasted bed as a mass vibration block. The validity of the model was verified by comparing the overall response of the numerical calculation of the ballasted bed and the field test results. Liu et al. [6] studied the effect of tamping operations on the vibration characteristics of ballasted track through an

* Corresponding author at: MOE Key Laboratory of High-speed Railway Engineering, Southwest Jiaotong University, Chengdu, China.
E-mail address: chenrong@home.swjtu.edu.cn (R. Chen).

https://doi.org/10.1016/j.conbuildmat.2021.125898
Received 12 June 2021; Received in revised form 29 October 2021; Accepted 25 November 2021
Available online 4 December 2021

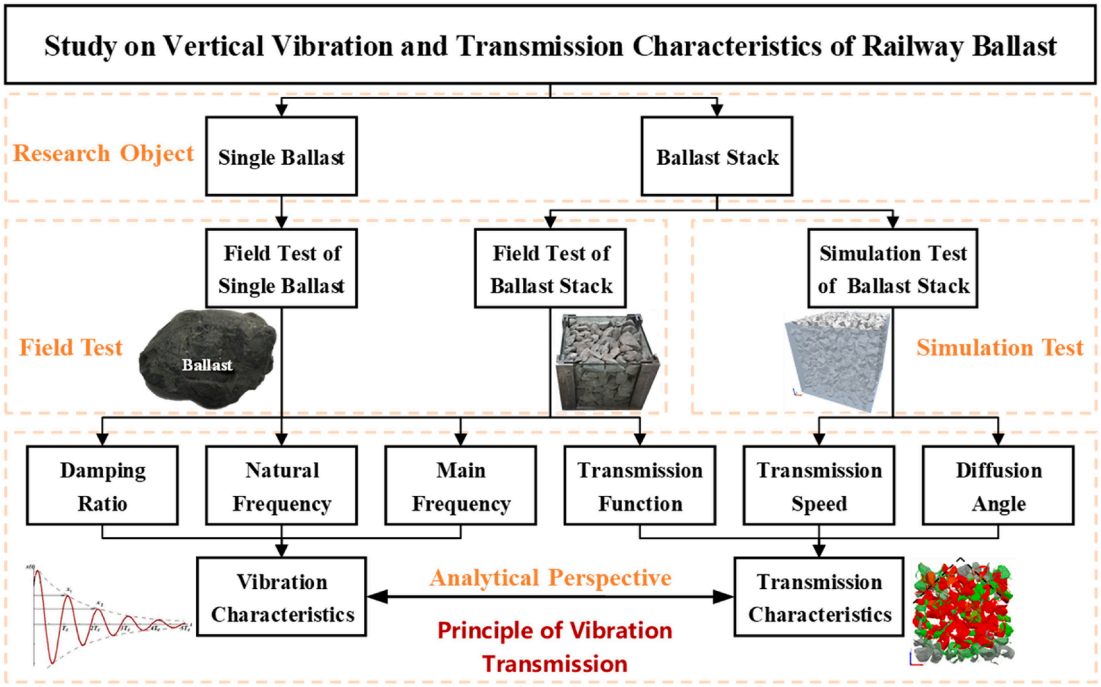

Fig. 1. Technology roadmap.

impact test and the finite element method (FEM). The above studies all treated a ballasted bed as equivalent to a continuum, and revealed the essence of its vibration characteristics.

Ballasted beds are formed by gravel particles, and their overall mechanical properties are closely related to the movement characteristics of ballast particles. Therefore, the introduction of the discrete element method (DEM), as proposed by Cundall [7–9], has opened a new horizon for the study of the granular mechanical properties of railway ballast. The rock landslide phenomenon was studied by comparing the results of actual field tests and numerical simulations. These were found to be highly consistent, and DEM could better reflect the bulk characteristics of rocks. In recent years, DEM has been widely used in the study of ballasted tracks, and is an important tool for revealing the vibration characteristics of ballasted beds. Gao et al. [10] used a ball element to establish a ballasted bed model, analyzed the vibration response of a ballasted bed under a vehicle load, and obtained its contact force transmission angle and depth attenuation law. Bian et al. [11] used polyhedrons to simulate irregularly shaped ballast particles, and established a discrete element model to study the dynamic response of a ballasted bed. The model successfully represented the dynamic characteristics of the track structure and soil cushion under a vehicle load.

The geometric topological structure of ballast particles has a strong degree of arbitrariness, and its arrangement in a ballasted stack is random. This is exhibited in a ballasted stack as state dependence on soft matter [12,13], giving it poor uniformity and strong dispersion, which makes it difficult to verify the microscopic vibration law of the discrete element model of a ballasted stack in terms of a field test. Because of the good correlation between shear wave velocity and compaction stiffness [14–16], in the maintenance of ballasted track, shear waves are often used to detect its quality. This method has strong engineering application value, but the vibration characteristics of ballast particles in ballasted tracks have not been studied yet. Guo et al. [17] used particle image velocimetry (PIV) to study the interaction mechanism between a ballasted bed and a sleeper under vibration load. The recent development of micro-embedded smart sensors has provided a solution for this problem [18,19]. Huang et al. [20] and Bian et al. [21] developed a SmartRock by embedding the smart chips of a triaxial accelerometer and a triaxial gyroscope in ballast. With the SmartRock, they studied the vibration characteristics of ballast during cyclic loading, obtaining good agreement between field tests and simulation results, and satisfactorily solved the monitoring problem of a ballasted bed. Milne et al. [22] studied the problem of ballast splashing caused by a passing train using embedding low-cost MEMS accelerometers in a single ballast particle. They identified the differences between the motion states of the ballast and the track superstructure. Aikawa et al. [23,24] buried a smart sensor in ballast and placed it in a ballasted bed. They studied the vibrations of the ballast particles and obtained the vibration characteristics of the ballasted bed in field tests. All the above studies used embedded sensors to study the vibration characteristics of ballasted beds, and they provide important references.

The impact hammer test is commonly used to study the vibration characteristics of ballast [25–27]. In this manuscript, a ballast sensor was constructed by embedding chips, and the correctness of the sensor was verified through a hammer excitation test. We continued to use the

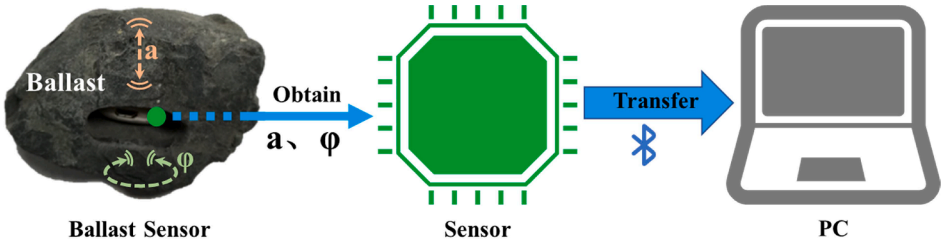

Fig. 2. Principles of ballast sensor.

Table 1
Sensor specifications.

Sensor	Model	Precision	Range	Sampling frequency
Accelerometer	BMI 160	0.001 g	±16 g	800 Hz
Gyro	BMI 160	0.001°/s	±2000°/s	800 Hz

impact hammer test to study the vertical vibration characteristics of the ballast particles and a ballasted stack. A numerical calculation model of a ballasted box was established based on DEM, and the transmission law of the ballasted stack was studied, as shown in Fig. 1.

2. Field test method

2.1. Test object

Intelligent chips of an integrated triaxial accelerometer, triaxial gyroscope, Bluetooth, and memory chip were embedded in an opening created at the center of gravity of a ballast particle. To eliminate relative motion between the development board and ballast particle, high-strength AB adhesive with a tensile shear strength of 12.4 MPa at room temperature was used in the packaging. The constructed device could sense the motion state of a ballast particle [28], as shown in Fig. 2.

The parameters of the accelerometer and gyroscope are shown in Table 1.

Four ballast particles meeting the Chinese special-grade requirements [29] were chosen, and their weights were measured and recorded as m_0. The four ballast particles were color-coded and made into ballast sensors by embedding chips in a hole opened at their centers of gravity. Their weights were measured and recorded as m_t, as shown in Fig. 3.

The percent changes of weight of the four ballast particles after being made into ballast sensors were 2.62%, 3.42%, 3.61%, and 2.93%, all less than the 5% allowable error of the experiment [30], so weight changes of ballast particles could be neglected.

2.2. Vertical axis calibration of ballast sensor

The ballast sensors were placed at random. After a ballast sensor came to rest and was stabilized, it was necessary to calibrate the coordinate system to ensure that its z-axis coincided with the direction of gravity [31,32].

The accelerations of the stationary sensor in the three axial directions are denoted as (a, b, c), so the direction vector is V = (a, b, c). The unit vector in the direction of gravity is Z = (0, 0, 1). The direction vector V of the ballast sensor can be rotated to coincide with the z-axis of the coordinate system through two coordinate rotations. The correction matrix is [28]

$$R = \begin{bmatrix} \frac{\sqrt{b^2+c^2}}{\sqrt{a^2+b^2+c^2}} & 0 & \frac{a}{\sqrt{a^2+b^2+c^2}} \\ -\frac{ab}{\sqrt{b^2+c^2}\sqrt{a^2+b^2+c^2}} & \frac{c}{\sqrt{b^2+c^2}} & \frac{b}{\sqrt{a^2+b^2+c^2}} \\ -\frac{ac}{\sqrt{b^2+c^2}\sqrt{a^2+b^2+c^2}} & -\frac{b}{\sqrt{b^2+c^2}} & \frac{c}{\sqrt{a^2+b^2+c^2}} \end{bmatrix} \quad (1)$$

The four manufactured ballast sensors could be used directly in the field test once the coordinate system was calibrated.

2.3. Feasibility analysis of ballast sensor

The sensor module and ballast sensor were placed on a horizontal rigid foundation, and a hammer was used to excite them with appropriate impact force, so that there was no obvious jump after they were excited, to prevent the sensor module or ballast sensor from bounces and slips that could interfere with the test. Ten valid tests were carried out for each working condition, and the acceleration data of the sensor module and ballast sensor were collected through a smartphone or PC.

Since the hammer excitation was different for each test, it was meaningless to analyze the time-domain characteristics of the test results, so their frequency-domain characteristics were analyzed. The normalized frequency-domain results of 10 repetitions under the two working conditions are shown in Fig. 4.

The results show that when the hammer is used to directly excite the sensor module and ballast sensor, they show multiple frequency peaks. When the hammer directly excites the sensor module, its frequency-domain response fluctuates greatly, with its main frequency peak at 67.78 Hz, and obvious peaks at 223.24 Hz and 342.50 Hz, but the amplitude difference at each peak frequency is small. When the hammer directly excites the ballast sensor, its main frequency peak is at 83.62 Hz,

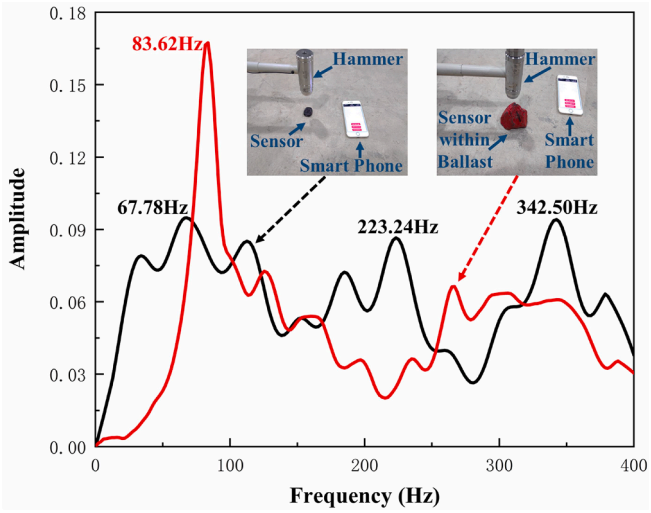

Fig. 4. Verification test of ballast sensor.

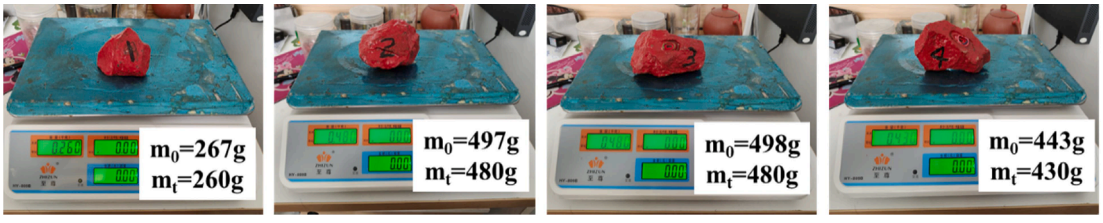

Fig. 3. Masses of ballast sensors.

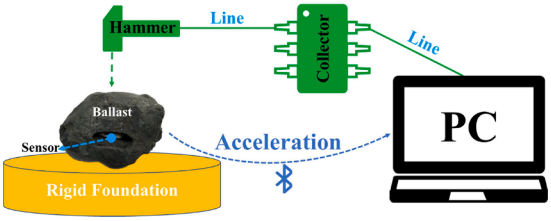

Fig. 5. Test method of single ballast.

and the amplitude corresponding to the main frequency is significantly different from the other peak frequencies. Comparing the frequency-domain curves, it can be seen that there is a large difference in their frequency domains of vibration. It can be considered that the ballast sensor and sensor module have different vibration characteristics. Therefore, it is feasible to use the ballast sensor to obtain the ballast vibration signal.

3. Impact hammer test of a single ballest particle

3.1. Test method

The four ballast sensors were placed in turn on a rigid base and excited by the hammer with an appropriate impact force, so that they did not jump significantly after being excited. Ten valid tests were carried out for each working condition. After the vibration of the ballast had dampened out, the excitation signal of the impact hammer was acquired with a collector. The response signals of the four ballast sensors were obtained by Bluetooth, as shown in Fig. 5.

After the tests, the ten test results under each working condition were normalized, and the vibration response signals of the ballast sensors under the working condition were obtained.

3.2. Analysis of test results

Fig. 6 shows the hammer excitation signals and the response signals of the ballast sensor from the four groups of tests.

With the excitation of the impact hammer, all four ballast sensors showed acceleration responses. The amplitude of the ballast sensor response was directly related to the magnitude of the impact force of the

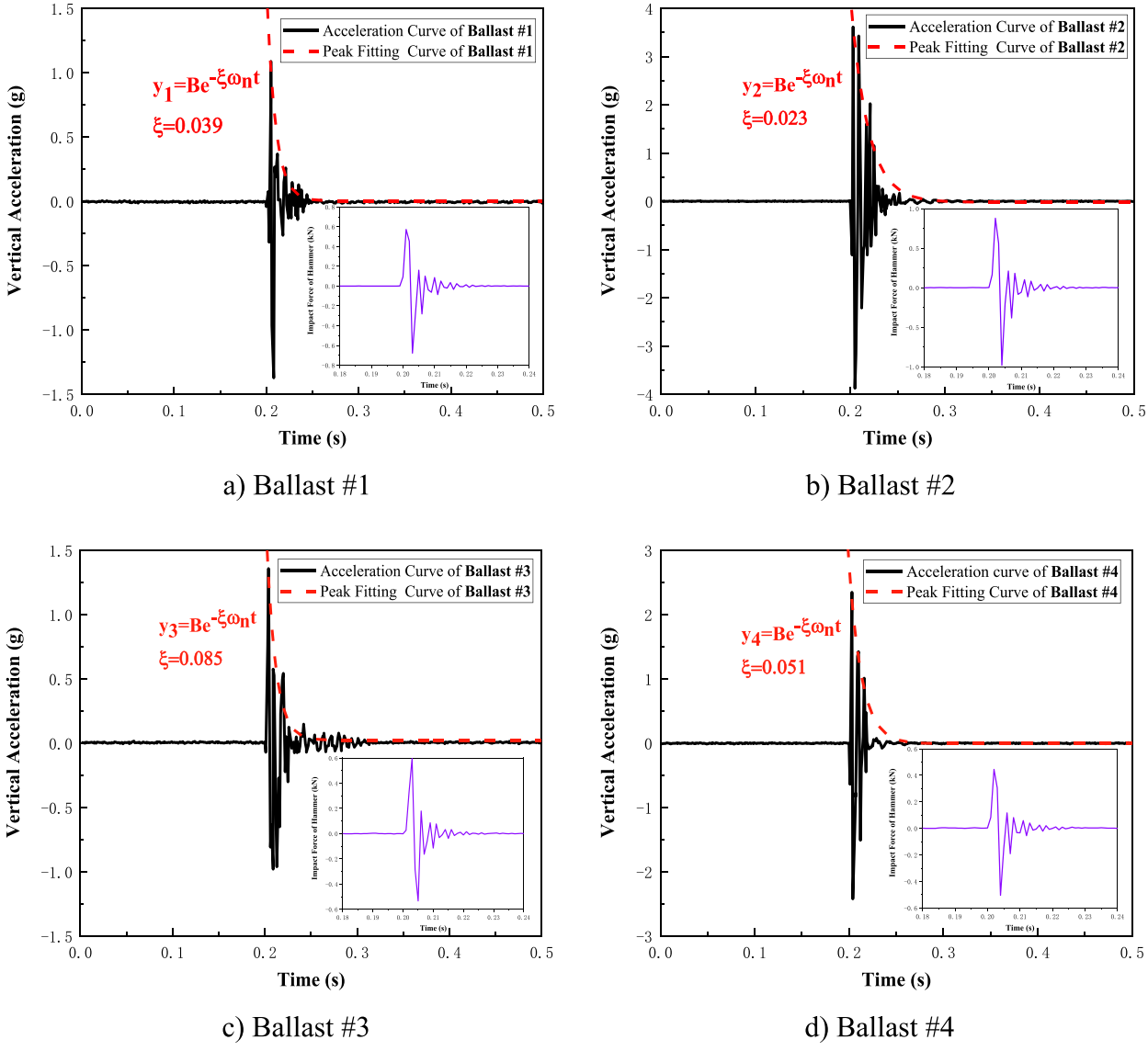

Fig. 6. Response signals of ballasts when struck individually.

Table 2
Damping vibration parameter table of single ballast response.

Ballast number	Coefficient of fitting curve		Damping vibration parameters	
	R^2	Adj R^2	ξ	ω_d
#1	0.984	0.983	0.039	2692.791
#2	0.941	0.940	0.023	2356.194
#3	0.966	0.965	0.085	1047.200
#4	0.987	0.987	0.051	1449.964

hammer. The response signals of each ballast gradually decreased until stabilized, which was nonharmonic motion, indicating that the ballast vibrated under the excitation of the force hammer on a rigid base, exhibiting distinct damping characteristics [33]. We analyze the test data through damped vibration theory.

The differential equation of damped vibration is [34]:

$$m\ddot{x} + c\dot{x} + kx = 0, \tag{2}$$

which is a second-order homogeneous linear differential equation, where k is the stiffness, c is the damping coefficient, and m is the mass. The damping ratio, or viscous damping factor, is

$$\xi = \frac{c}{2\sqrt{km}} \tag{3}$$

This is the ratio of the damping coefficient of the material to the critical damping coefficient, and it indicates how fast the vibration of the material decays [35]. For common small damping materials in engineering, $0 < \xi$ less than 1. So, for the corresponding homogeneous equation, equation (2) has the general solution

$$x = Be^{-\xi\omega_0 t}\sin(\omega_d + \varphi) \tag{4}$$

Equation (4) shows that the damped vibration consists of an amplitude $Be^{-\xi\omega_0 t}$ that decays according to an exponential law, and a periodic function with a natural frequency ω_d. B is an undetermined coefficient, φ is the phase, and ω_0 is the natural circular frequency of the corresponding undamped vibration,

$$\omega_0 = \sqrt{\frac{k}{m}} \tag{5}$$

The natural frequency of the system is

$$\omega_d = \omega_0\sqrt{1-\xi^2} \tag{6}$$

The relationship between the natural frequency ω_d and vibration period T_d of the system is

$$T_d = \frac{2\pi}{\omega_d} \tag{7}$$

On the time history curve of the ballast in response, 10 consecutive cycles were selected for observation, and the total time duration was recorded as

$$T_d = \frac{t}{10} \tag{8}$$

Curve fitting was performed on the peak values of each time history curve, as shown in Fig. 6, and the damping ratio ξ and natural frequency ω_d of the four ballast sensors under the excitation of the hammer can be calculated by equations (2)–(8), with results as shown in Table 2.

In Table 2, R2 is the determination coefficient, and Adj R^2 is the adjusted determination coefficient. According to the principle of the determination coefficient by curve fitting [36], Adj R^2 and R^2 were both close to 1, and the difference between them was less than 0.2, indicating that all coefficients of the fitted curves are reliable, and the curves have a high degree of precision.

The damping ratios of the four ballast sensors with the excitation of the hammer were all less than 0.1, confirming that the ballast materials have a small damping ratio. All the natural frequencies were above 1000 Hz, indicating that the resonance frequencies of the ballast particles were high. Through the modal analysis of FEM, it was found that the first-order modal frequency of a single ballast was above 1000 Hz [37]. The vibration characteristics of ballasts are greatly affected by the texture and friction of the particle surface. In a ballasted stack, the particle shape, gradation, and bulk density will all have a significant impact on its vibration [38].

Due to the effects of the mass, shape, materials, and environmental factors [39], the damping ratio and natural frequency of the four ballast particles showed considerable variation. Fig. 3 shows that ballast sensors #2 and #3 have the same mass, but considerably different damping ratios and natural frequencies. This indicates that the shape of the ballast has a greater effect on the damping ratio and the natural frequency.

4. Impact hammer test of ballasted stack

To study the vibration characteristics and the transmission rate of the ballasted stack, an impact hammer test was carried out on a ballasted stack. The test result was analyzed in both the time and frequency domains. The result was compared with those described in section 3 to reveal the law of vibration transmission in a ballasted stack.

4.1. Test method

Considering the standard thickness of a ballasted bed [40], a ballasted box with a length of 360 mm was established. Its main support structure was constructed with 20-mm steel plates, and for ease of observing the ballast motion and to avoid friction between the boundary and the ballast, the four sidewalls of the box were made of smooth 10-mm tempered glass. Ballast sensors #1 through #4 were placed from

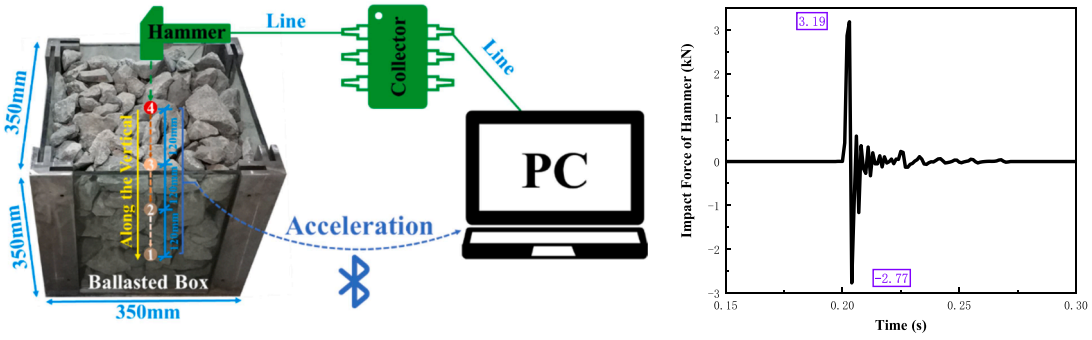

a) Field test method b) Time history curve of hammer excitation

Fig. 7. Test method of ballasted stack.

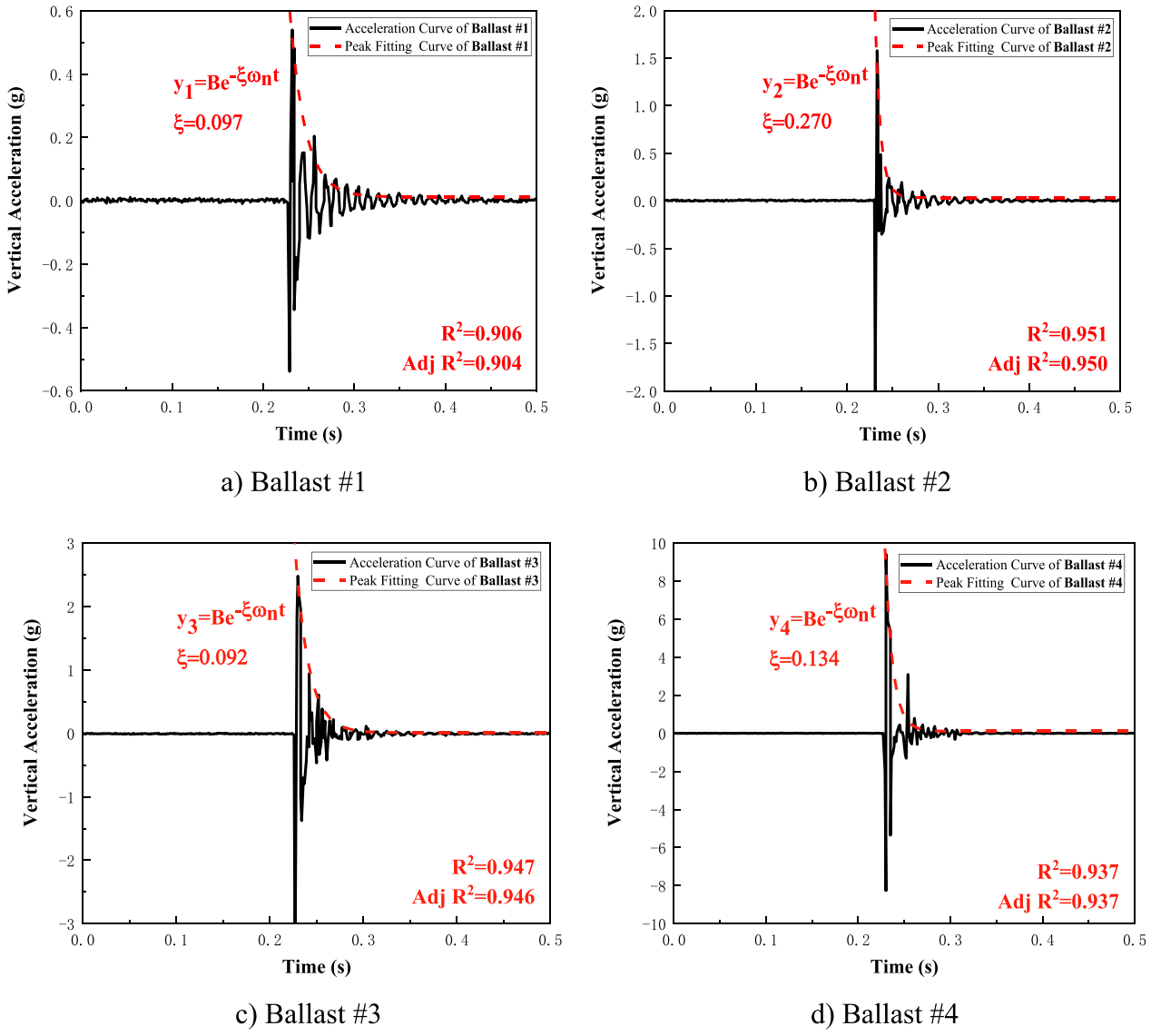

Fig. 8. Time-domain curves of acceleration response of ballasted stack.

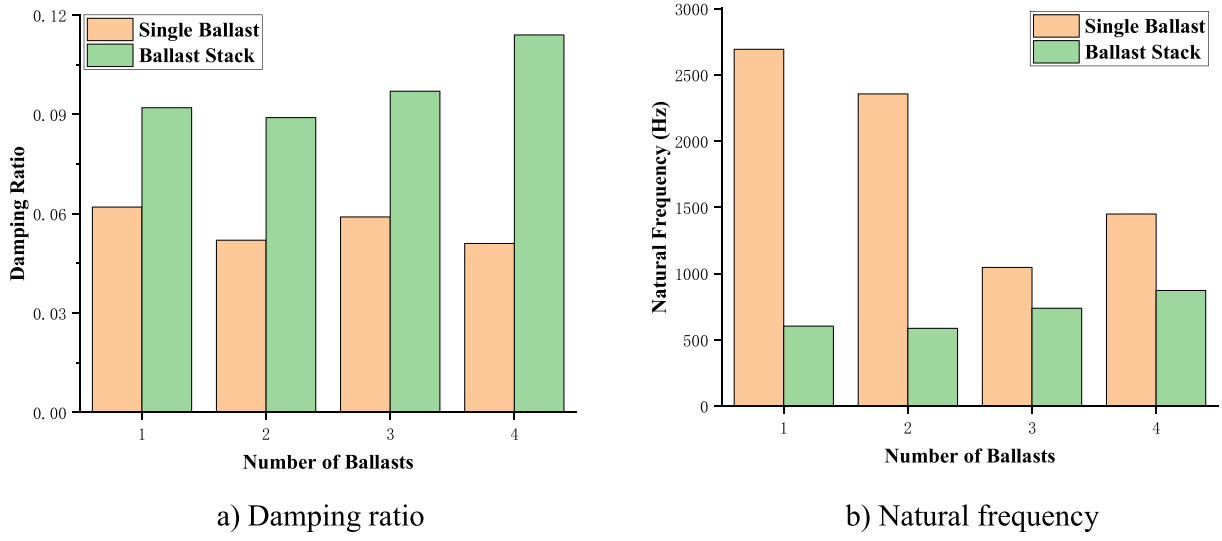

Fig. 9. Difference in vibration parameters.

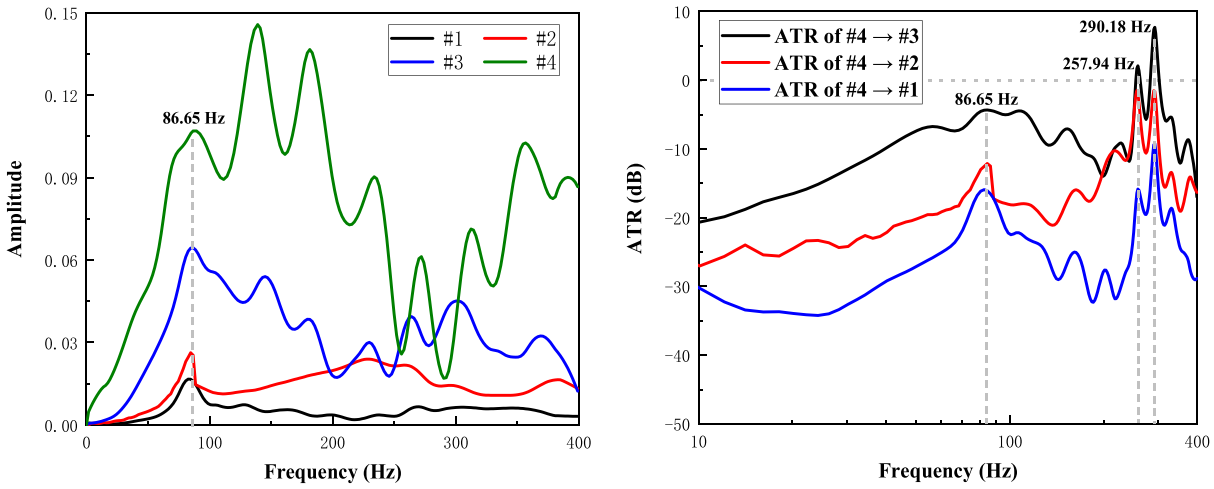

a) Frequency-domain signal in ballasted box b) ATR of ballasts in ballasted box

Fig. 10. Frequency-domain characteristics of ballasted stack.

the top to the bottom, at the center of the box, at intervals of 12 cm. The acceleration data of the four ballast sensors were acquired from the box in real time using a smartphone or PC with Bluetooth transmission. The test box was filled with Chinese special-grade ballast, and the bulk density of the ballasted stack was measured [41] to be 1.73 g/cm^3.

During the test, ballast sensor #4, on the top surface of the box, was struck forcefully. The excitation signal of the impact hammer and the vertical acceleration response signals of the four ballast sensors were acquired in the manner described in section 3.1, as shown in Fig. 7.

4.2. Time domain analysis of test results

After the test, the time history curves of the acceleration response of the four ballast sensors arranged in the depth direction were extracted, as shown in Fig. 8.

When exciting by the hammer, the four ballast sensors began to vibrate in order, from top to bottom. Since sensor #4 was struck directly by the hammer, its vibration amplitude was the greatest. Because the vibration energy dissipated during transmission, the vibration amplitude sensed by the four ballast sensors gradually decreased with increasing depth, with the amplitude sensed by ballast sensor #1 at the bottom of the box being the smallest.

Fig. 8 shows that the response signals of the four ballast sensors arranged along the depth in the box still showed the characteristics of damped vibration. Using the analysis method described in section 3.2, the peaks of the time-domain response signals of the four ballast sensors were analyzed. Compared to Table 2, the parameters of the damped vibration in a single ballast particle and in the ballasted stack are shown in Fig. 9.

Fig. 9 shows that when excited by the hammer, the damping ratios sensed by the four ballast sensors in the stack were all greater than that sensed by a single ballast particle. This indicates that the stack state of ballast changes the damping characteristics of the ballast particles and makes vibration attenuation more likely to occur. Of the four ballast sensors, the damping ratio sensed by ballast sensor #4 at the top of the box showed the greatest amplitude variation. This indicates that the lower ballasted layer provides good elastic support, reflecting the soft material attribute of the ballasted stack.

The natural frequencies of the four ballast sensors in the box were between 600 Hz and 900 Hz, all smaller than that of a single ballast particle. The stack state of ballast has a significant influence on its natural frequency, which makes a ballasted stack more prone to structural resonance with load excitation. At different vertical depths in the stack, the natural frequency of the ballast varied very little, but ballast sensor #3, at a depth of 12 cm at the center of the box, showed the lowest natural frequency, so resonance is most likely to occur at sensor #3.

4.3. Frequency domain analysis of test results

The response signals of the four ballast sensors in the box were analyzed with Fourier transforms, and the frequency-domain signals could be obtained. To explore the transmission characteristics of the vertical vibration in the ballasted box, we define the acceleration transmission rate (ATR) [42] as the transmission function of acceleration A_n of ballasts #3, #2, and #1 along the depth direction, and acceleration A of ballast #4 at the top of the text chamber, after it receives the vibration load [43], which is usually expressed in logarithmic form as

$$ATR = 20\lg[H(A_n, A)], n = 1, 2, 3\cdots, \quad (9)$$

where H(A_n, A) is the amplitude of the transfer function between input A and output A_n. It can be seen from Equation (9) that a positive ATR indicates that the amplitude of the transfer function is greater than 1, i.e., the output vibration is more severe than the input at the current frequency.

The frequency-domain characteristics and ATR of the four ballast sensors in the box are shown in Fig. 10.

Fig. 10 a) shows that after the excitation of the hammer, the main frequency of the vibration in sensor #1, located 36 cm from the surface, was about 86.65 Hz. This shows that the main frequency of the response signal at the bottom of the box should be 86.65 Hz. Ballast sensors #2 through #4 had a number of frequency peaks. In summary, 86.65 Hz is the main frequency of the vertical vibration of the ballasted stack in the box.

Fig. 10 b) shows that below 86.65 Hz, the ATR fluctuated with an increasing trend as the frequency increased. This is because, after each ballast sensor started vibrating, the amplitude fluctuated to overcome the constraint of the stack environment until the vibration reached the main frequency. Between 86.65 Hz and 257.94 Hz, the ATR first decreased, and then it increased sharply. This indicates that the vertical vibration of the ballasted stack was particularly affected at 257.94 Hz. At 257.94 Hz and 290.18 Hz, the ATR from ballast #4 to ballast #3 was greater than zero, indicating that a ballast within a depth of 12 cm from the top surface of the box was greatly affected by the hammer excitation. The ATR from ballast #4 to ballasts #2 and #1 gradually decreased,

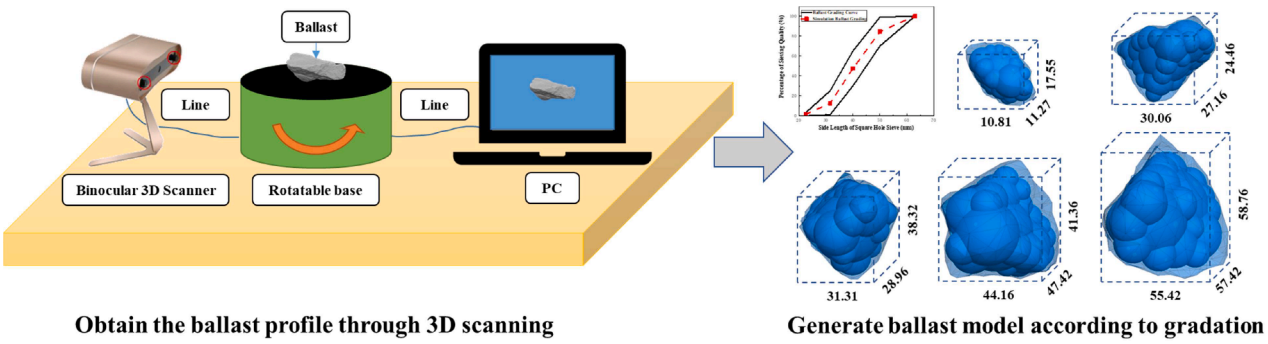

Fig. 11. Generating a discrete element ballast model.

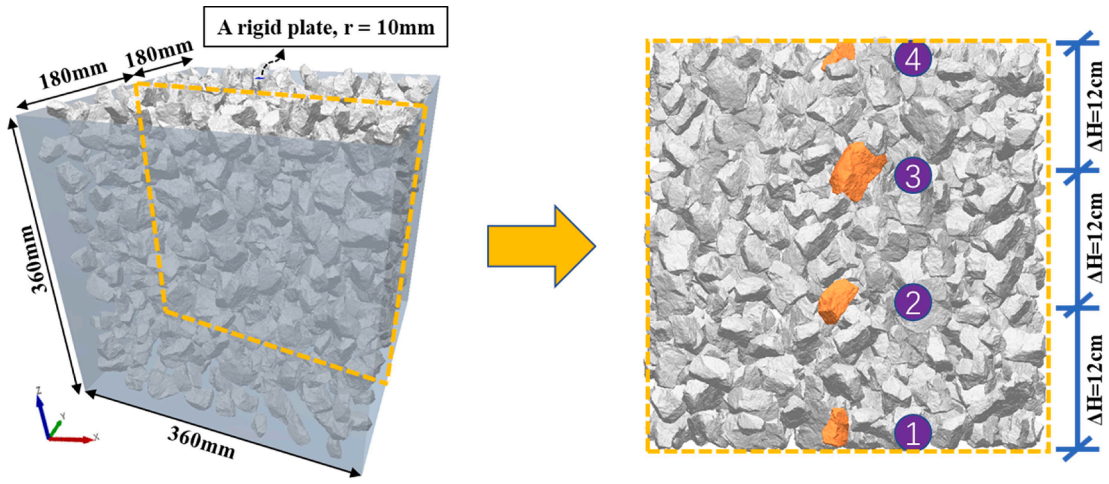

Fig. 12. Discrete element model of ballasted box.

indicating that the thickness of the ballasted stack was correlated with vibration damping performance.

The ATR of the ballasts was lower at frequencies below 257.94 Hz than at frequencies above 257.94 Hz. From this, we know that the vibration damping performance of a ballasted bed is better in a low frequency range than in a high frequency range.

5. Transmission law of ballasted stack based on DEM

To further reveal the transmission behavior of the ballasted stack excited by a hammer, we established a discrete element numerical calculation model for the ballasted box that was consistent with the scale and material of the field test.

5.1. Building a discrete element numerical model

The profile of typical ballasts that meet the Chinese special-grade was acquired using a 3D scanner, and its accuracy was optimized [44]. To build a discrete element ballast model, the 3D ballast profile was filled using the ball clump method [45]. On average, it took 20 balls to fill a ballast, and the numerical calculation requirements were fulfilled [46], as shown in Fig. 11.

We established a discrete element numerical model with the same dimensions as the field test in section 4.1. The top of the model was a circular rigid plate with a radius of 10 mm. With this, an impact load was applied to the ballasted stack of the simulation model, as shown in Fig. 12.

Since the Hertz-Mindlin constitutive model [47–49] can efficiently and accurately calculate the nonlinear contact force between ballasts, it was chosen for discrete element numerical calculation. The parameters used in the numerical calculation are shown in Table 3 [50,51].

Table 3
Discrete element simulation parameters.

Parameter	Value
Poisson's ratio	0.24
Density	2600 kg/m^3
Young's modulus	5.45 × 10^{10} Pa
Collision restitution coefficient	0.72
Coefficient of static friction	0.56
Coefficient of rolling friction	0.27

The simulation test box was filled with ballast particles that met the Chinese special-grade, and through layered tamping, the bulk density of the box was controlled at 1.73 g/cm^3. A total of 882 ballasts were used. After the numerical calculation was completed, one ballast was selected every 12 cm along the central axis of the box, from top to bottom, and designated for analysis, as shown in Fig. 12.

5.2. Verification of discrete element numerical model

In the DEM model, a hammer impact such as shown in Fig. 7 b) was applied to the rigid plate. Using the post-processing module of the DEM simulation software, the vertical acceleration of the four designated ballasts was analyzed, as shown in Table 4.

The results of Table 4 show that the simulation results were very close to those of the field test. Unlike the numerical simulation, the field test relied on humans to maintain the direction of the hammer load as close to vertical as possible. Additionally, the stacking of the ballasts in the box had a certain randomness, so the numerical simulation could not

Table 4
Peak and valley values of vertical acceleration of ballast (unit: g).

	#1		#2		#3		#4	
	Peak	Valley	Peak	Valley	Peak	Valley	Peak	Valley
Simulation	0.57	0.52	1.56	2.13	2.37	4.11	9.78	8.07
Field Test	0.54	0.54	1.58	2.04	2.48	3.95	9.42	8.25
Difference	5.56%	3.70%	1.27%	4.41%	4.44%	4.05%	3.82%	2.18%

Table 5
Cloud map of ballasted stack.

Time (μs)	Cloud Map	Time (μs)	Cloud Map
1	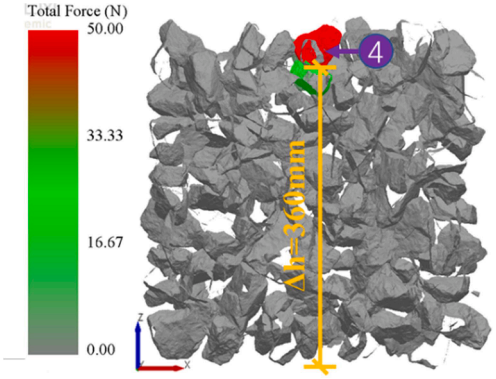	225	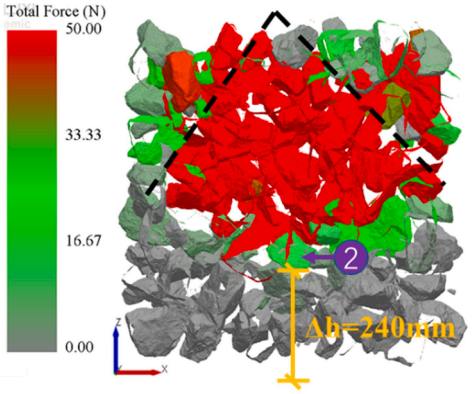
53	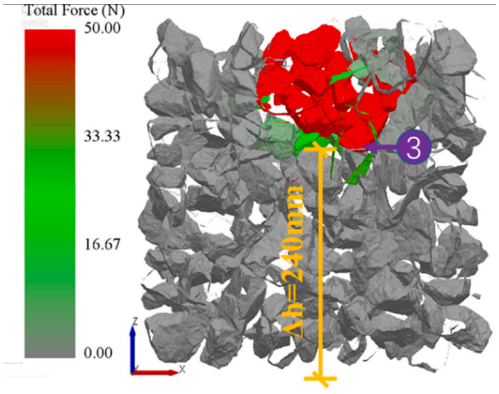	407	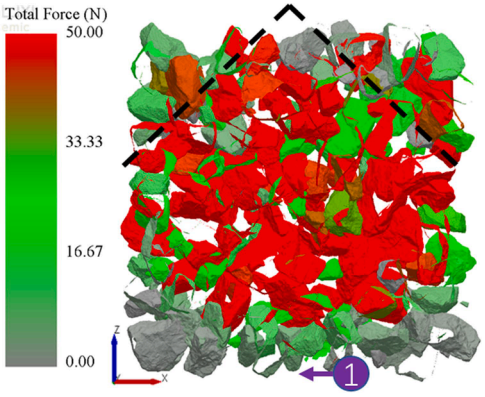

be in total agreement with the field test.

Since the amplitudes of the numerically simulated vertical acceleration of the four ballasts were consistent with the results of the field test, and the line shapes were in agreement, the simulation model was validated.

5.3. Transmission characteristics of ballasted stack

In the DEM model, we observed the cloud map of the ballasted stack at each time step. The corresponding cloud maps at the moments when the vibration load first acted on ballasts #4, #3, #2, and #1 were counted, as shown in Table 5.

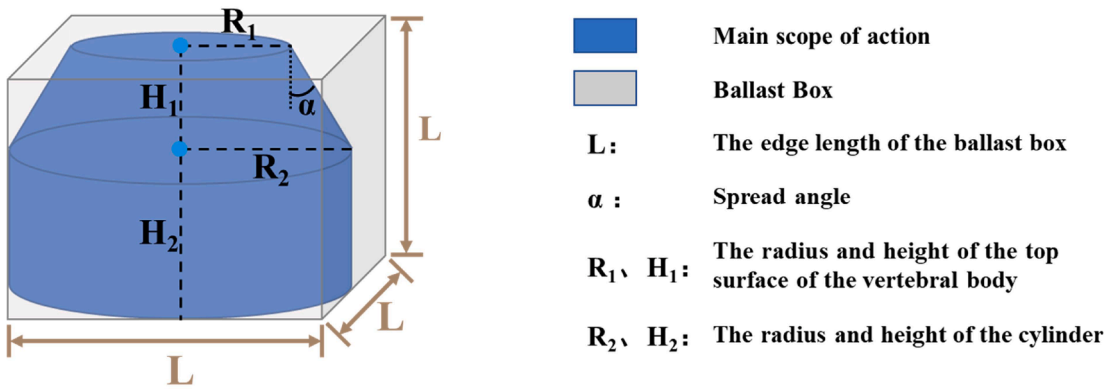

Fig. 13. Main influence scope of hammer excitation.

As the depth increased, the vertical vibration transmission speed of the ballast and the accumulated external force gradually decreased. From the results shown in Table 5, the average vertical vibration transmission speed was calculated to be 0.88 mm/μs, and the ballast vibration was transmitted downward at a diffusion angle of 35.32°–54.51° from the direction of gravity.

We used a statistical method to study the effect area of the vibration load on the ballasted box. Since the maximum impact force of the hammer was 5.96 kN, each ballast particle in the box bore an average load of 6.75 N of external force. Ballast particles with a maximum total external force greater than 6.75 N were designated as main load-bearing ballasts. We extracted the time history data of the external force received by each ballast in the simulated ballasted box, and drew the main influence scope diagram of the hammer excitation, as shown in Fig. 13.

In the numerical simulation, R_1 was 53.67 mm. Taking the median of the diffusion angle to be 44.92°, the volume of the main influence scope was calculated to be 64.80% of the total volume of the ballasted box. This indicates that the excitation load of the hammer was mainly borne by 64.80% of the ballast in the box.

It should be noted that in Fig. 13, the top surface radius R_1 of the vertebral body and the diffusion angle in the box were greatly affected by the bulk density. The more porous the top layer of the ballast was, the smaller R_1 was; and the more uniform the bulk density was, the more regular the bottom surface of the ballast was. Since the size of the box was finite, reflection and dissipation of energy existed at its boundary. The author intends to conduct an in-depth study on the above phenomenon.

6. Conclusion

A ballast sensor was constructed by embedding chips, and the correctness of a ballast sensor was verified through an impact hammer test. We used the impact hammer test to study the vertical vibration characteristics of ballast particles and a ballasted stack. A numerical calculation model of the ballasted box was established based on DEM, and the transmission law of the ballasted stack was studied. The results show that:

(1) The damping ratio of the ballast particles is less than 0.1, which makes the ballast a low damping material. The natural frequency is above 1000 Hz.
(2) The damping ratio and natural frequency of ballasts are greatly affected by their shape.
(3) The damping ratio of a ballasted stack is greater than that of the ballast particles, and its natural frequency is lower. This indicates that the ballasted stack has the attributes of a soft material.
(4) The ATR of the ballasts is lower at frequencies below 257.94 Hz than that at frequencies above 257.94 Hz. This indicates that the vibration damping performance of a ballasted bed is better in a low frequency range than in a high frequency range.
(5) As the depth increases, the vertical vibration transmission speed of the ballast gradually decreases, as does the accumulated external force. In the impact hammer test of a ballasted box, the average vertical vibration transmission speed was calculated to be 0.88 mm/μs, and the ballast vibration was transmitted downward at a diffusion angle of 35.32°–54.51° from the direction of gravity.

Declaration of Competing Interest

The authors declare that they have no known competing financial interests or personal relationships that could have appeared to influence the work reported in this paper.

References

[1] C. Esveld, Modern Railway Track, 2nd Editon, Delft university of Technology, 2001.
[2] B. Indraratna, W. Salim, C. Rujikiatkamjorn, Advanced rail geotechnology - ballasted track. Advanced Rail Geotechnology - Ballasted Track, 2011.
[3] A.B.U. Sayeed M, M.A. Shahin, Three-dimensional numerical modelling of ballasted railway track foundations for high-speed trains with special reference to critical speed, Transport. Geotechn. 6 (2016) 55–65.
[4] L. Li, S. Nimbalkar, R. Zhong, Finite element model of ballasted railway with infinite boundaries considering effects of moving train loads and Rayleigh waves, Soil Dyn. Earthquake Eng. 114 (2018) 147–153.
[5] W. ZHAI, X. SUN, A DETAILED MODEL FOR INVESTIGATING VERTICAL INTERACTION BETWEEN RAILWAY VEHICLE AND TRACK, Veh. Syst. Dyn. 23 (sup1) (1994) 603–615.
[6] J. Liu, P. Wang, G. Liu, et al., Influence of a tamping operation on the vibrational characteristics and resistance-evolution law of a ballasted bed, Constr. Build. Mater. 239 (2020).
[7] P.A. Cundall, The measurement and analysis of accelerations in rock slopes, University of London, 1971.
[8] P.A. Cundall, A computer model for simulating progressive large-scale movements in blocky rock systems, Proc.int.symp.on Rock Fracture 1(ii-b):11–8 (1971).
[9] P.A. Cundall, O.D.L. Strack, A Discrete Numerical Mode For Granular Assemblies, Géotechnique 29 (1) (1979) 47–65.
[10] H. Xiao, L. Gao, B.W. Hou, Analysis of ballast dynamic behavior with three-dimensional discrete element method, Journal of Railway Engineering Society 26 (9) (2009) 14–17, https://doi.org/10.3969/j.issn.1006-2106.2009.09.004, in Chinese.
[11] Bian XC, Li W, Li GY, Erol Tutumluer. Three-dimensional discrete element analysis of railway ballast's shear process based on particles' real geometry [J]. Engineering Mechanics,2015,32(05):64-75+83. (In Chinese).
[12] T.Y. Zhou, B. Hu, P. Xu, B. Yan, Numerical Study on the Evolution of Force Chain inside Railway Ballast under Tamping Operation, Applied Mechanics & Materials 724 (2015) 275–278.
[13] W-X. Xu, H-G. SUN, W. CHEN, et al., A review of correlative modeling for transport properties, microstructures, and compositions of granular materials in soft matter, Acta Physica Sinica 65 (17) (2016).
[14] M. Zagyapan, C.A. Fairfield, Continuous surface wave and impact methods of measuring the stiffness and density of railway ballast, NDT and E Int. 35 (2) (2002) 75–81.
[15] P. Anbazhagan, B. Indraratna, C. Rujikiatkamjorn, L. Su, Using a seismic survey to measure the shear modulus of clean and fouled ballast, Geomech. Geoeng. 5 (2) (2010) 117–126.
[16] H.-J. Hwang, H.-C. Park, Evaluation of condition of gravel ballast layer on high-speed railway using surface wave method based on harmonic wavelet analysis of waves, NDT and E Int. 68 (2014) 78–87.
[17] Y. Guo, W. Jia, V. Markine, G. Jing, Rheology study of ballast-sleeper interaction with particle image Velocimetry (PIV) and discrete element modelling (DEM), Constr. Build. Mater. 282 (2021) 122710, https://doi.org/10.1016/j.conbuildmat.2021.122710.
[18] M. Gao, P. Wang, L. Jiang, B. Wang, Y. Yao, S. Liu, D. Chu, W. Cheng, Y. Lu, Power generation for wearable systems, Energy Environ. Sci. 14 (4) (2021) 2114–2157.
[19] M. Gao, J. Cong, J. Xiao, Q. He, S. Li, Y. Wang, Y. Yao, R. Chen, P. Wang, Dynamic modeling and experimental investigation of self-powered sensor nodes for freight rail transport, Appl. Energy 257 (2020) 113969, https://doi.org/10.1016/j.apenergy.2019.113969.
[20] S. Liu, H. Huang, T. Qiu, L. Gao, Comparison of Laboratory Testing Using SmartRock and Discrete Element Modeling of Ballast Particle Movement, J. Mater. Civ. Eng. 29 (3) (2017), https://doi.org/10.1061/(ASCE)MT.1943-5533.0001540.
[21] K. Zeng, T. Qiu, X. Bian, M. Xiao, H. Huang, Identification of ballast condition using SmartRock and pattern recognition, Constr. Build. Mater. 221 (2019) 50–59.
[22] D. Milne, L. Pen, G. Watson, et al., Measuring Acceleration of Ballast Particles at Track Level[C], Third International Conference on Railway Technology: Research, Development and Maintenance (2016).
[23] A. AIKAWA, Techniques to Measure Effects of Passing Trains on Dynamic Pressure Applied to Sleeper Bottoms and Dynamic Behavior of Ballast Stones, Quarterly Report of Rtri 50 (2) (2009) 102–109.
[24] A. Aikawa, Vertical Natural Vibration Modes of Ballasted Railway Track, in: H. Yalciner, E. Noroozinejad Farsangi (Eds.), New Trends in Structural Engineering, IntechOpen, 2018, https://doi.org/10.5772/intechopen.79738.
[25] H.F. Lam, M.T. Wong, Railway Ballast Diagnose through Impact Hammer Test[C], Procedia Eng. 14 (2011) 185–194.
[26] R. De Bold, D.P. Connolly, S. Patience, M. Lim, M.C. Forde, Using impulse response testing to examine ballast fouling of a railway trackbed, Constr. Build. Mater. 274 (2021) 121888, https://doi.org/10.1016/j.conbuildmat.2020.121888.
[27] H. Wu, L. Zhu, W. Song, Z. Xu, F. Xu, H. Gong, Impact performance of ballast by incorporating waste tire-derived aggregates, Constr. Build. Mater. 288 (2021) 122992, https://doi.org/10.1016/j.conbuildmat.2021.122992.
[28] G. Liu, P. Li, P. Wang, J. Liu, J. Xiao, R. Chen, X. Wei, Study on structural health monitoring of vertical vibration of ballasted track in high-speed railway, J. Civil Struct. Health Monitor. 11 (2) (2021) 451–463.
[29] National Railway Administration of People's Republic of China. TB/T 2140-2018, Railway ballast[S]. China Railway Publishing House Co., LDT.
[30] A.S. Morris, R. Langari, Statistical analysis of measurements subject to random errors, in: Measurement and Instrumentation, Elsevier, 2021, pp. 75–132.

[31] S. Cho, B.F. Spencer, Sensor attitude correction of wireless sensor network for acceleration-based monitoring of civil structures, Comput. Aided Civil Infrastruct. Eng. 30 (11) (2015) 859–871.
[32] G. Morgenthal, H. Höpfner, The application of smartphones to measuring transient structural displacements. Journal of Civil, Struct. Health Monitor. 2 (3-4) (2012) 149–161.
[33] W.M. Zhai, K.Y. Wang, J.H. Lin, Modelling and experiment of railway ballast vibrations, J. Sound Vib. 270 (4-5) (2004) 673–683.
[34] W.T. Thomson, Theory of Vibration with Applications, 5th ed., Tsinghua University Press, Beijing, 2005.
[35] M.D. Binder, N. Hirokawa, U. Windhorst, Damping Ratio, Springer, Berlin, 2008.
[36] H. Bar-Gera, The Target Parameter of Adjusted R-Squared in Fixed-Design Experiments, Am. Stat. 71 (2) (2017) 112–119.
[37] A. Aikawa, Determination of dynamic ballast characteristics under transient impact loading, Electron. J. Struct. Eng. 13 (1) (2013) 17–34.
[38] B. Indraratna, Y. Sun, S. Nimbalkar, Laboratory assessment of the role of particle size distribution on the deformation and degradation of ballast under cyclic loading, J. Geotech. Geoenviron. Eng. 142 (7) (2016) 04016016, https://doi.org/10.1061/(ASCE)GT.1943-5606.0001463.
[39] W. Gao, Natural frequency and modal shape analysis of structures with uncertainty, Mech. Syst. Sig. Process. 21 (1) (2007) 24–39.
[40] National Railway Administration of People's Republic of China.TB 10082-2017, Code for Design of Railway Track.China Railway Publishing House Co., LDT.
[41] E.T. Selig, T.S. Yoo, H.M. Chen, E.T. Selig, Railroad Ballast Density Measurement. Astm, Geotech. Test. J. 1 (1) (1978) 41, https://doi.org/10.1520/GTJ10367J.
[42] Sheng X. Vibration Transmission Characteristics and Control Measures of Track Structure. Southwest Jiaotong University, 2019. (In Chinese).
[43] S. Kaewunruen, A.M. Remennikov, Field trials for dynamic characteristics of railway track and its components using impact excitation technique, NDT and E Int. 40 (7) (2007) 510–519.
[44] J. Liu, J. Xiao, H. Liu, G. Liu, P. Wang, Y. Lin, Random generation method of ballast 2D topology based on particle characteristics, Constr. Build. Mater. 221 (2019) 762–771.
[45] M. Lu, G.R. McDowell, Discrete element modelling of ballast abrasion, Géotechnique 56 (9) (2006) 651–655.
[46] W.L. Lim, G.R. McDowell, Discrete element modelling of railway ballast, Granular Matter 7 (1) (2005) 19–29.
[47] H. Hertz, On the contact of elastic solids, Journal für die reine und angewandte Mathematik (Crelles Journal) 92 (156) (1880).
[48] R.D. Mindlin, Compliance of elastic bodies in contact, J. Appl. Mech. 16 (1949) 259–268.
[49] R.D. Mindlin, H. Deresiewicz, Elastic Spheres in Contact Under Varying Oblique Forces, J.appl.mech.asme 20 (3) (1953) 327–344.
[50] J.-L. Xiao, G.-Z. Liu, J.-X. Liu, J.-C. Dai, H. Liu, P. Wang, Parameters of a discrete element ballasted bed model based on a response surface method, J. Zhejiang Univer.-Sci. A 20 (9) (2019) 685–700.
[51] Y. Guo, C. Zhao, V. Markine, G. Jing, W. Zhai, Calibration for discrete element modelling of railway ballast: A review, Transp. Geotech. 23 (2020) 100341, https://doi.org/10.1016/j.trgeo.2020.100341.